Journal of Non-Crystalline Solids 600 (2023) 122032

Contents lists available at ScienceDirect

Journal of Non-Crystalline Solids

journal homepage: www.elsevier.com/locate/jnoncrysol

Microstructural evaluation and mechanical properties of bulk nanostructured $Al_{86}Cu_6Y_6La_2$ (at.%) alloy produced by hot consolidation of amorphous melt-spun flakes

M. Dadashi, M. Salehi *, S.G. Shabestari

School of Metallurgy and Materials Engineering, Iran University of Science and Technology (IUST), Tehran, Iran

ARTICLE INFO

Keywords:
Aluminum alloy
Amorphous alloy
Nanocrystalline material
Stress/strain measurement
Thermal analysis

ABSTRACT

Amorphous melt- spun $Al_{86}Cu_6Y_6La_2$ (at.%) alloy is hot consolidated at $T = 723$ K and $P = 700$ MPa. The glassy ribbons show three devitrification steps which fcc-Al phase is precipitated during the first crystallization stage, and formation of intermetallic compounds (Al_3Y, AlCu, $AlCu_3$ and Al_3Y_5) take place in the next steps. The calculated Avrami exponent ($n \sim 2.6$) shows the first crystallization reaction is governed by the diffusional growth process and increasing nucleation rate. Moreover, the activation energy calculated with different methods show that E_a for the primary crystallization are in the range of about 254- 267 KJ.mol^{-1}. Amorphous ribbons exhibit a remarkably tensile strength of 910 ± 7 MPa. Combined rapid solidification and hot consolidation produce a bulk sample with high hardness (345.1 ± 12.3 HV), compressive strength (460 ± 10 MPa) and 4 pct plastic strain. These high mechanical properties are due to ultrafine microstructure induced by the rapid solidification process.

1. Introduction

Metallic glasses with high Al contents have attracted great attention because of their high mechanical properties. Non-equilibrium conditions of an amorphous structure can increase their properties considerably. Melt-spun amorphous Al ribbons show high tensile strengths exceeding 1200 MPa, which is about twice as high as for conventional crystalline Al alloys [1–3].

Directly rapid solidification or following devitrification of the melt-spun amorphous ribbons leads to an evenly distributed nanoscale phase in the amorphous matrix, which results in enhancement of the tensile fracture strengths even more [4–7]. The defect-free nanometer fcc-Al precipitates in the amorphous matrix results in the high strength of the alloys due to dispersion strengthening. Structural heterogeneities formed in the amorphous matrix increase the number of shear bands. Therefore, plasticity is improved and fast growth of the local shear bands is suppressed by nanoparticles [8,9]. Enhancement of solute contents of the amorphous matrix also is a key parameter in the high strength of the nanocrystalline- amorphous composite material [10].

The Al metallic glasses produced by non-equilibrium processes have small dimensions in the form of powders or ribbons because Al alloys are marginal glass formers. Therefore, consolidation techniques are required in order to produce a bulk sample for possible structural application. High cooling rates (10^5–10^6 Ks^{-1}) is required to bypass devitrification. Therefore, rapid solidification methods are essential to produce amorphous structures [2,4,6,8]. However, Al-based amorphous alloys with thickness in the range of mm was obtained via copper mold casting for Al based alloy [1,2]. Therefore, Al-based amorphous alloys with high mechanical properties have limited application fields due to their size limitation [11–13].

To overcome the size limitation, rapid solidification combined with powder metallurgy (RS/PM) processing techniques have been applied to produce bulk Al-based samples with the desired microstructure which can significantly improve the mechanical properties of aluminum alloys [1,14]. Densification and softening the material can be reached through high pressure and rather high temperature, allowing better filling and removing the remaining porosity due to plastic deformation. In addition, in order to better bonding, particles slide or shear over each other resulting in disintegrating oxide and other surface layers [15].

Crystallization studies of the metallic glasses has a principal effect on the area of the amorphous and nanostructured alloy. Controlled crystallization of the glassy precursors, which improves their mechanical properties, requires detailed understanding of the mechanism of the nanocrystalline particles formation influencing structural

* Corresponding author.
E-mail address: maryamsalehi@iust.ac.ir (M. Salehi).

https://doi.org/10.1016/j.jnoncrysol.2022.122032
Received 4 July 2022; Received in revised form 13 October 2022; Accepted 8 November 2022
Available online 16 November 2022

transformations [16–19]. The risk of possible crystallization during high temperature exposure is the most important problem of consolidation of the amorphous alloys. The proper consolidation parameters (i.e. consolidation time and temperature) are required in order to produce a highly dense sample, where the coarsening of the microstructure is inhibited during crystallization of the alloy [20].

Although many efforts have been made in the field of the Al-TM (Ni)-RE metallic glasses [2,4,21-25], there is little study about Al-Cu-RE alloys. Addition of the rare earth (RE) elements increases the thermal stability of the Al-Cu alloys. Therefore, high temperature strength and stiffness of this alloy system will be increased [26]. A long solidification range, dispersion hardening and thermally stable structure leads to high casting and mechanical properties of the novel Al-Cu-Y alloys [27]. In this study, hot pressing (HP) of the amorphous $Al_{86}Cu_6Y_6La_2$ flakes results in a novel bulk Al based alloy with a nano/ultra-fine structure which significantly improves their thermal stability and mechanical properties. Microhardness, tensile and compression tests have been used in order to evaluate the mechanical behavior of the as- cast, as- spun and consolidated bulk samples revealing promising mechanical properties. Moreover, the crystallization kinetics as well as the phase and microstructure transformation of an amorphous alloy were studied. The results are correlated to the microstructural changes and mechanical behavior of this alloy.

2. Experimental procedure

2.1. Melt spinning and hot consolidation process

The alloy $Al_{86}Cu_6Y_6La_2$ (at.%) was produced by vacuum induction melting of a combination of pure Al (99.99 wt%), Cu (99.99 wt%), Y (99.99 wt%), and La (99.99 wt%) elements in a quartz crucible under a high purity argon gas environment. Three times remelting of the ingot is lead to obtain compositional uniformity. A single roll melt spinning machine was used to produce amorphous ribbons with about 1–2 mm width and 15 μm thickness. The bulk samples are produced through consolidation of the amorphous flakes in two steps: (1) the as-spun flakes inside a die cold pressed at room temperature (RT) as pre-consolidation process in order to produce a green compact sample for 10 min and (2) the green samples are hot pressed (HP) at a heating rate of 20 $Kmin^{-1}$ and time of 20 min. The conditions of the consolidation process are listed in Table 1. The amorphous flakes were consolidated into approximately 7 mm height and 10 mm diameter rod by a uniaxial WEBER PWW machine.

2.2. Structural characterization and mechanical evaluation

DSC analysis (Mettler Toledo) has been used in order to study the thermal stability and crystallization behavior of the melt-spun ribbons. A few flakes were heated at heating rates of 10, 15 and 20 $Kmin^{-1}$ from room temperature to 900 K in the Argon atmosphere. Philips, PW1800, Cu-Kα (λ =1.54 Å) X-ray device was used to investigate the structural evaluation of the rapidly solidified amorphous, annealed and bulk samples (30 mA, 40 kV) [10]. Structural investigations were studied by standard metallographic techniques. The chemical etchant was modified Keller's solution, which was used for about 5 s. A Neophot 32 optical microscope was used for characterization of the resultant cross-sectional microstructures of the melt-spun specimen. The FE-SEM (15 kV) attached to an energy dispersive spectrometry (EDS Silicon Drift 2017) was also used. The hardness of the samples has been measured by a MVK-H21 microhardness tester at loads of 25 g (ribbons) and 100 g (as-cast and bulk samples) and at 15 s dwelling time. The measurements have been done on the longitudinal sections of the ribbons. A SANTAM 50 uniaxial tensile test was also used at a strain rate of $5 \times 10^{-4}\ s^{-1}$ to study the mechanical properties of the amorphous as-spun ribbons. Moreover, an INSTRON 8562 testing facility (strain rate of $1 \times 10^{-4}\ s^{-1}$) was performed in order to evaluate the compression behavior of the as- cast and bulk samples (with parallel surfaces at both ends) at RT.

Table 1
Experimental conditions of consolidation process of the amorphous $Al_{86}Cu_6Y_6La_2$ flakes.

Bulk Sample	Cold pressing condition	Hot pressing condition
Sample 1	P = 800 MPa	T = 693 K (420 °C), P = 600 MPa
Sample 2	P = 1 GPa	T = 723 K (450 °C), P = 700 MPa

3. Results

3.1. X-ray diffraction and thermal analysis of RS ribbons

The XRD patterns of the $Al_{86}Cu_6Y_6La_2$ (at.%) alloy at as- cast, as-spun and annealed conditions at different temperatures corresponding to the different crystallization stages are shown in Fig. 1. The results show that the as-spun alloy has a broad diffuse peak in the 32–48° range, which suggests completely amorphous alloys (Fig. 1a). The rapid solidification process is beneficial to formation of the amorphous structure.

As- spun ribbons were heat- treated into partially and completely crystallized state after annealing at 610, 720 and 790 K and heating rate of 20 $Kmin^{-1}$ to reveal the crystallization products. The annealing temperature and time were determined based on the nonisothermal DSC curves shown in Fig. 2. XRD pattern obtained from the partially crystallized sample at 610 K (about the last point of the first DSC curve), indicates that the fcc α-Al nanoparticles are precipitated during the first crystallization reaction (Fig. 1c). Whereas, the matrix is decomposed into intermetallic compounds of Al_3Y, $AlCu_3$, Al_3Y_5 during non-isothermal heating of the $Al_{86}Cu_6Y_6La_2$ alloy at 720 K (Fig. 1d). In addition, AlCu phase and some unidentified phases appear after complete devitrification at 790 K (Fig. 1e). The peak intensity of the α-Al phase increases during the second and complete crystallization, indicating the growth of fcc α-Al nanocrystals.

Fig. 2 indicates the DSC curves of the as-solidified ribbons at 10, 15 and 20 $Kmin^{-1}$ heating rates and non-isothermal conditions. DSC curves show three exothermic crystallization peaks (T_x) which is usual for Al-TM-RE metallic glasses mostly. It is important to note the crystallization can be quite sensitive to composition [24]. All of the peaks are shifted to a higher temperature as the heating rate is increased and their intensity extended. This is due to the assumption that the crystallization is a thermally activated process. Table 2 presents the crystallization and peak temperatures (T_{X1}, T_{X2}, T_{X3}, T_{P1}, T_{P2}, T_{P3}) for $Al_{86}Cu_6Y_6La_2$ alloy from the DSC curves at various heating rates. An endothermic peak as glass transition (T_g) can be observed in the DSC patterns of some alloys [28]. In some alloy systems, crystallization takes place first and T_x appears before T_g. Therefore, T_g has vanished. Table 2 also shows T_g and ΔT_X, (supercooled liquid region which shows the temperature region between T_g and T_{x1}) for various heating rates.

3.2. Consolidation of RS flakes

Fig. 3 indicates the XRD curve of the bulk sample prepared by consolidation of RS $Al_{86}Cu_6Y_6La_2$ flakes via uniaxial hot pressing. Full densified bulk sample is achieved at T= 723 K (450 °C) and P= 700 MPa. The XRD pattern of the 10 mm diameter rod shows formation of crystalline phases including α-Al, Al_3Y, AlCu, $AlCu_3$, Al_3Y_5 and some undefined phases. Although the pressing temperature (723 K)is lower than the third DSC peak temperature (765 K at heating rate of 20 $Kmin^{-1}$), the amorphous structure devitrified completely may be due to the deformation induced crystallization effect. The inset of Fig. 3 indicates the bulk sample with height of about 7 mm.

3.3. Microstructural evolution and mechanical properties

The cross-sectional microstructure of the as-cast, as-spun and

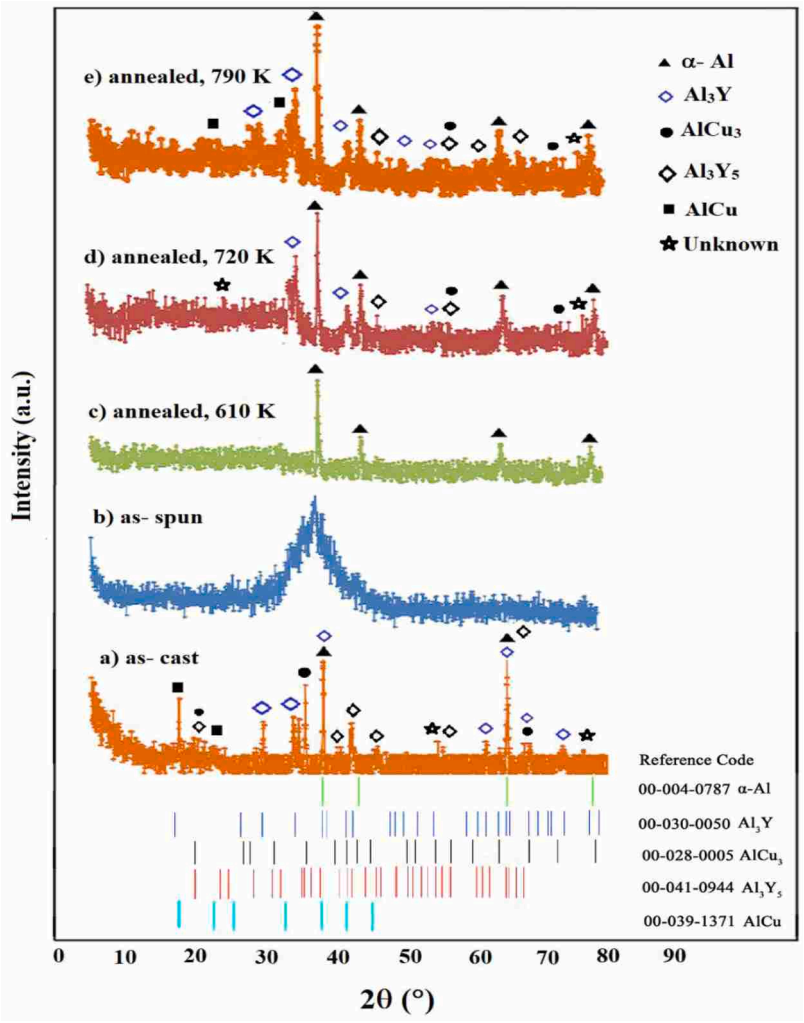

Fig. 1. XRD patterns for the $Al_{86}Cu_6Y_6La_2$ (at.%) alloy at (a) as- cast, (b) as-spun and (c-e) annealed conditions at different temperatures.

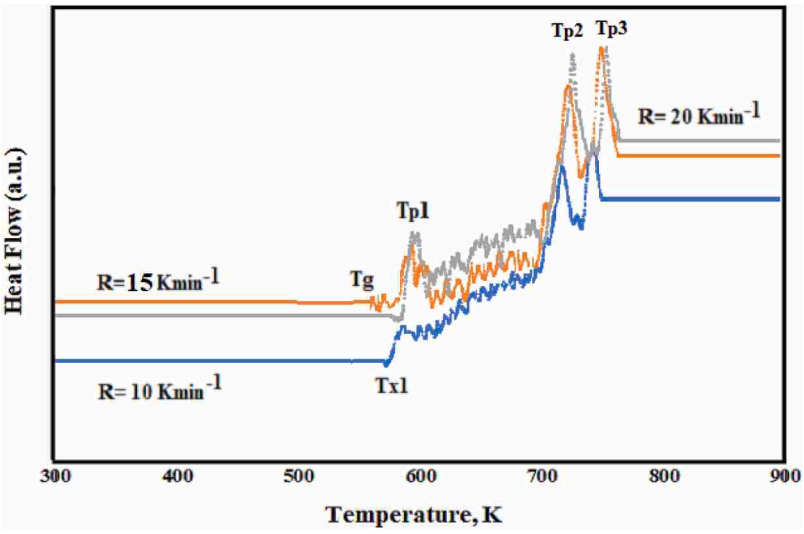

Fig. 2. The non-isothermal DSC curves at 10, 15, and 20 $Kmin^{-1}$ heating rates.

consolidated samples obtained by optical microscopy can be shown in Fig. 4. The primary aluminum solid solution (α-Al) and a fine eutectic were the main structure parts of the Al-Cu-Y based alloy system [29]. Fig. 4a shows the microstructure of the slowly solidified (as-cast) $Al_{86}Cu_6Y_6La_2$ sample consists of white region of α- Al phase, fine gray-colored eutectic phase and some dark acicular and blocky shape

Table 2
Characteristic temperatures and supercooled liquid region for $Al_{86}Cu_6Y_6La_2$ alloy.

β (K/min)	T_g (K)	T_X (K)			T_P (K)			ΔT_X
		T_{X1}	T_{X2}	Tx3	T_{P1}	T_{P2}	Tp3	
10	561	585	700	752	592	722	760	24
15	568	592	704	759	604	724	768	24
20	571	596	707	765	606	727	772	25

regions of Cu and RE (Y, La) bearing intermetallic phases. The presence of different phases (α-Al, Al_3Y, AlCu, $AlCu_3$, Al_3Y_5 and some undefined phases) in the as-cast sample was confirmed by XRD (Fig. 1a). However, the structure of the melt-spun ribbon (red arrows show its cross section) was quite different from those of the ingot specimens (Fig. 4b) indicating fine microstructure which is evaluated by FE-SEM (Fig. 5). Moreover, Fig. 4c and 4d show the optical microscopy of the compact materials hot consolidated at two conditions ($T = 693$ K, $P = 600$ MPa and $T = 723$ K, $P = 700$ MPa). Dark contrast in the sample is hot pressed at $T = 693$ K and $P = 600$ MPa (Fig. 4c) shows that complete metallic bonding has not been created between flakes in some sections. Arrows in Fig. 4c indicates the interfaces between the melt- spun flakes. However, optical microscopy of the bulk sample produced at T= 723 and P= 700 MPa shows a fully densified condition (Fig. 4d).

FE-SEM was also used to study the microstructure of the as-cast, as-spun, annealed and hot pressed samples at T= 723 and P= 700 MPa (Fig. 5). The microstructure of the as- cast sample consists of micro-sized particles with black contrast mostly concentrated along the grain boundaries and some bright particles embedded into the gray grains (Fig. 5a). The X-ray mapping images (Fig. 5b) indicate that the phases with gray color are aluminum solid solution and bearing RE (La, Y) eutectic phases (region 2) and the white (region 1) and black phases (region 3) are Cu, Y and La- rich intermetallic phases. Moreover, there isn't any trace of presence of crystalline phase in the matrix according to the longitudinal cross section of the as- spun ribbons (Fig. 5c) indicating a fully amorphous structure. The XRD pattern also approves this condition (Fig. 1a). The FE-SEM image of the $Al_{86}Cu_6Y_6La_2$ ribbons heat treated at 610 K (about end at first DSC peak) indicates homogeneously distributed fine nanoparticles in an amorphous matrix (Fig. 5d). The EDS patterns verify α-Al crystalline phase formation, which is also predicted by XRD result (Fig. 1b). The relatively inaccurate analysis of small phases by EDS and effect of matrix composition in the analysis leads to possible detestation of some other crystalline phases in the EDS analysis. The fcc α-Al nanocrystals emerge as the fine bright phases in the black amorphous matrix. The shape of α-Al particles is mostly uniaxial in the annealed ribbons.

Fig. 5e shows FE-SEM image of the bulk sample sintered at T= 723 and P= 700 MPa. The image shows bright particles and black rod-like regions with nm- sized dimensions. Fig. 5f shows the image prepared by Clemex analysis of the bulk sample indicating average size of the α-Al particles (164 nm). According to X-ray mapping analysis of bulk sample (Fig. 6) black particles in Fig. 5e suggested to be nano-sized Al grains and bright agglomerates rich in Cu, Co, Y and La, most likely corresponding to the $Al_{11}RE$, AL_3Y, Al_2Cu and AlCu compounds observed by XRD (Fig. 3).

Fig. 7 shows the hardness values of the $Al_{86}Cu_6Y_6La_2$ samples at as-cast, as- spun and after HP at $T = 723$ K and $P = 700$ MPa. It is clear that the amorphous alloy shows higher hardness value than as cast sample. The amorphous melt-spun alloy shows a microhardness of about 362.4 ± 11.4 HV, which is about more than two times with respect to conventional cast samples. Moreover, the hardness changes during the crystallization stages after the HP process, where, during primary crystallization, the hardness increases because of α- al nanoparticles. Third crystallization reaction of the alloy leads to a decrease of the hardness to 280.1 ± 10.4 HV. Growth of the α-Al nanoparticles, some weak intermetallic compounds and fully crystallization of the amorphous matrix may contribute to decrease the hardness after complete crystallization. Moreover, the hardness of the bulk consolidated sample at 723 K and P = 700 MPa reaches to 345.1 ± 12.3 HV which is more than two times that of conventional cast one due to ultrafine grain structure induced by rapid solidification process in the final bulk sample.

The tensile stress – strain curve of the amorphous $Al_{86}Cu_6Y_6La_2$ RS ribbons is shown in Fig. 8a. In order to minimize damaging gripping effects, pneumatic grips with smooth surfaces were used. Proof stress is determined as the stress corresponding to 0.2% of strain from the stress-strain curve of the ribbon. Yield strength (YS) and ultimate tensile strength (UTS) are 680±21 and 910 ± 18 MPa, respectively. However, the plastic deformation is small for the amorphous melt- spun ribbon. The result of the compression test of the as cast and bulk samples are

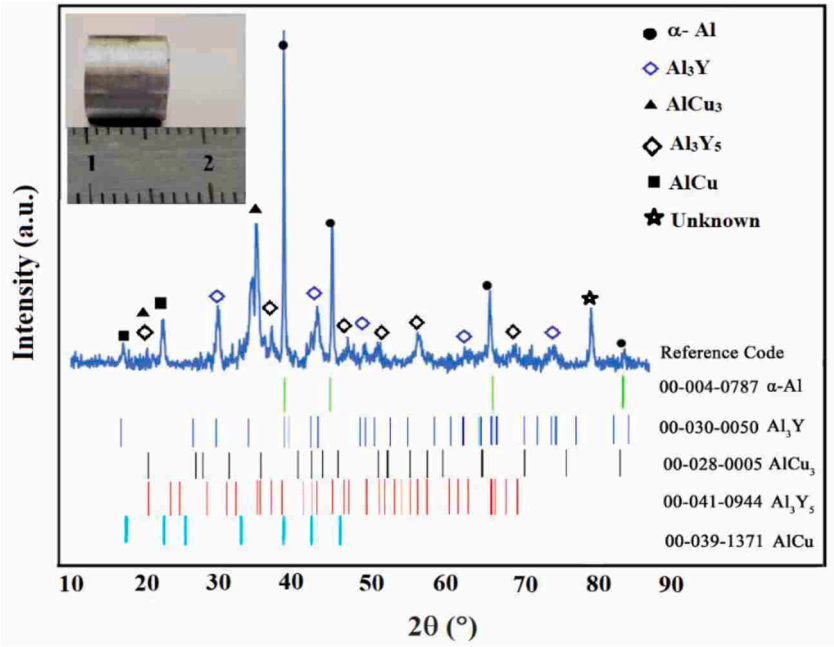

Fig. 3. XRD pattern of the melt-spun $Al_{86}Cu_6Y_6La_2$ flakes hot pressed at T= 723 K (450 °C) and P= 700 MPa. The inset is the appearance of the bulk sample.

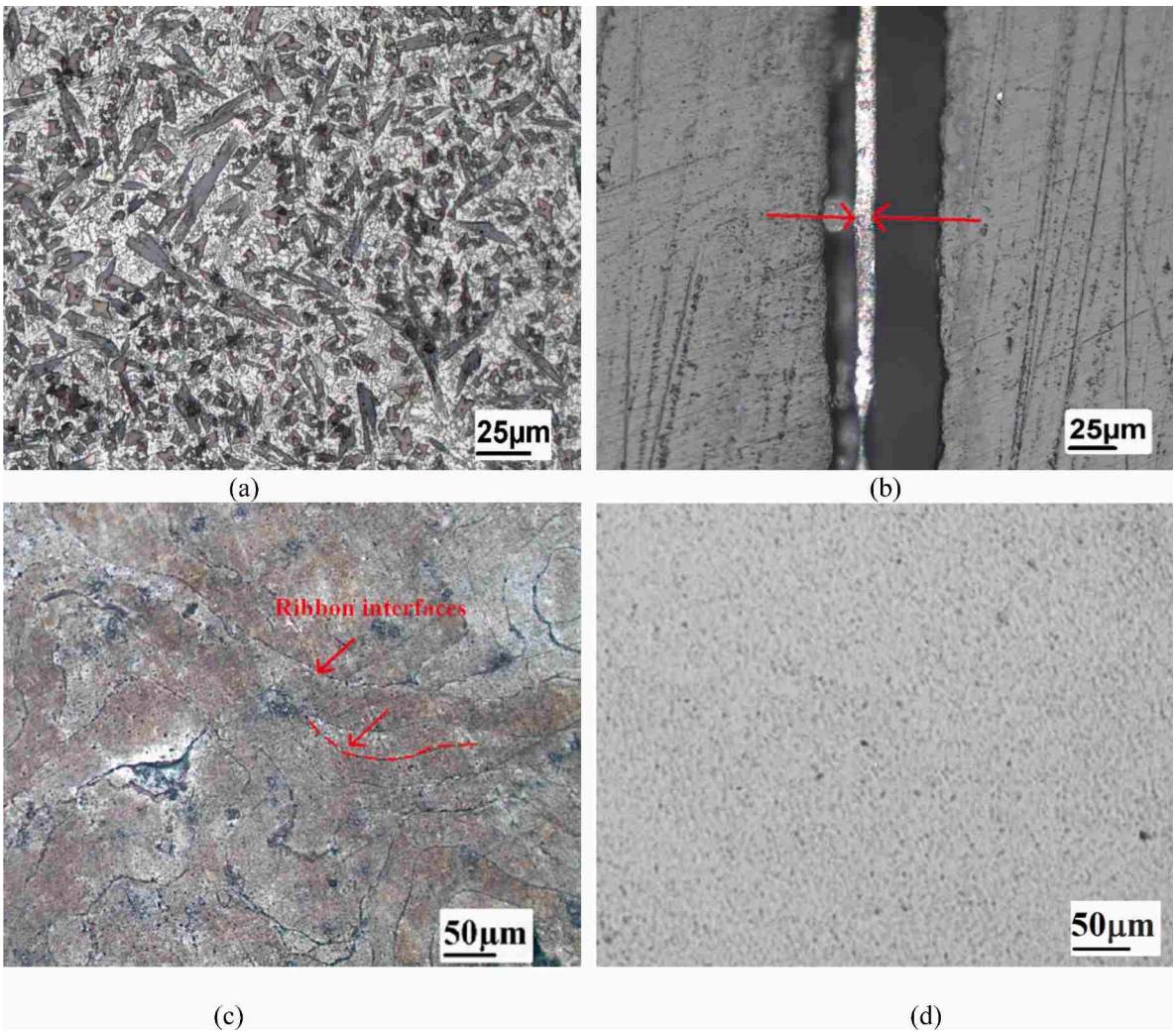

Fig. 4. Optical micrographs (prepared from the cross section) of the $Al_{86}Cu_6Y_6La_2$ alloy at different conditions: (a) as cast, (b) as spun, (c) hot pressed at $T = 693$ K and $P = 600$ MPa and (d) hot consolidated at $T = 723$ K, $P = 700$ MPa.

shown in Fig. 8b. The HP sample consolidated at pressing conditions of $T = 723$ K and $P = 700$ MPa, shows 460 ± 10 MPa yield strength and about 4 pct plastic strain. However, a yield strength of 184 ± 10 MPa and about 10 pct plastic strain can be seen in the as- cast sample. Ultrafine intermetallic phases, which uniformly distributed together with the nanocrystalline Al particles due to rapid solidification, is attributed to high mechanical properties of bulk samples. Structural refinement is also another parameter to increase the mechanical properties of rapidly solidified and hot consolidated bulk samples.

4. Discussion

4.1. Crystallization behavior and thermal stability of RS ribbons

The as-spun ribbons of the $Al_{86}Cu_6Y_6La_2$ alloy are fully amorphous due to the broad diffuse peak in the 2θ range of 32 to 48° (Fig. 1(a)). In the condition that the heat of mixing and atomic size mismatch between the main elements (Al, Cu and RE (Y, La) atoms) of the multicomponent systems are large, good glass forming ability (GFA) can be predicted. Size of the crystal unit cell increases by addition of more elements. Therefore, a complex structure will produce which reduces the tendency of formation of a structure with longer-range order. Existence of the large atoms enhances the packing density factor and therefore the energetic profit of remaining the sort range ordered structure. Moreover, the small bond Al–Cu length decreases the shear viscosity of the molten alloy. Therefore, the nucleation process is postponed and randomly ordered RE (Y, La) atoms [30–32] stabilize the amorphous structure. FE-SEM image of the as- spun ribbons (Fig. 5a) indicates no crystal to appear which is the characteristic of a completely amorphous structure.

Annealing of the as-spun ribbons at different temperatures corresponding to each DSC stage (610, 720 and 790 K) shows different crystallization products. During the primary crystallization, a phase of one of the alloy constituents appears first after the devitrification process. According to the XRD studies, α-Al nanoparticles are precipitated during the first crystallization reaction (Fig. 1c); whereas, intermetallic compounds (Al_3Y, $AlCu_3$, AlCu and Al_3Y_5) are formed in the matrix during non-isothermal heating of the $Al_{86}Cu_6Y_6La_2$ alloy after complete crystallization. The primary crystallized phase dispersed evenly in the amorphous matrix may act as the nucleation site for secondary or tertiary crystallization [24]. Precipitation of the α-Al crystalline phase embedded in the amorphous matrix is also verified by the FE-SEM image (Fig. 5b). This is also approved by the XRD pattern (Fig. 1c).

DSC analysis has been used in order to study the thermal stability of the Al amorphous ribbons. Supercooled liquid stability which is determined as $\Delta T_x = T_{X1} - T_g$ is a clearly described criteria for this purpose [33] which is >50 K for the most bulk metallic glasses. This often is less than 30 K in the Al metallic glasses, which are marginal glass formers [34]. According to Table 2, ΔT_X of $Al_{86}Cu_6Y_6La_2$ amorphous ribbons is in the range of 24–25 K for different heating rates which is comparable with 24 K reported for $Al_{86}Ni_6Y_6Ce_2$ (at.%) amorphous alloy [24]. This

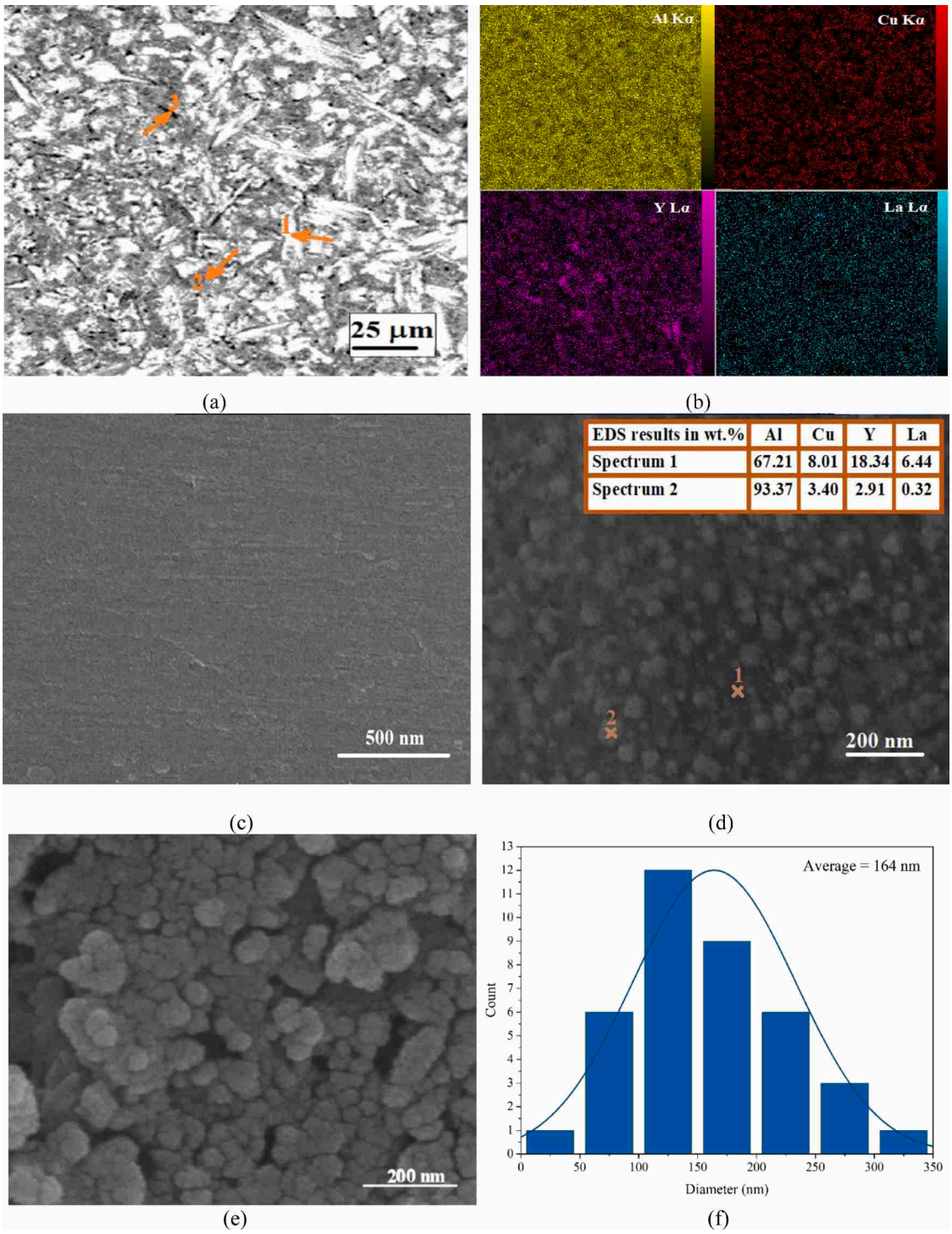

Fig. 5. FE-SEM images of $Al_{86}Cu_6Y_6La_2$ alloy at condition of: (a) as-cast (b) with corresponding X-ray mapping analysis, (c) as- spun, (d) heat-treated at 610 K (temperature of the first crystallization stage) with corresponding EDS spectrums and (e) bulk sample consolidated via hot pressed at T= 773 and P= 700 MPa showing grain and (f) image prepared by Clemex image analysis of bulk sample indicating average size of the α-Al particles.

indicates high thermal stability and GFA of the produced amorphous alloy due to difficulty in the nucleation and growth process. In this research, the onset crystallization temperatures are found to be in the range of 596- 765 K at different cooling rates. However, complete crystallization happens at approximately 795 K. The main parameters responsible for the high T_{x1} of the as- spun alloy are related to the large atomic size mismatch and negative ΔH_{mixing} between the constituents resulting in the complexity of the system. Large RE (Y and La) atoms lead atoms to move with difficulty and formation of the amorphous structure [34].

Principal crystallization process is investigated through calculation of the apparent activation energy E_a and thermal stability of the amorphous materials in this study. There are many approaches to compute the E_a of the metallic glasses including Kissinger, Ozawa, Augis & Bennett and Moynihan methods [35–38]:

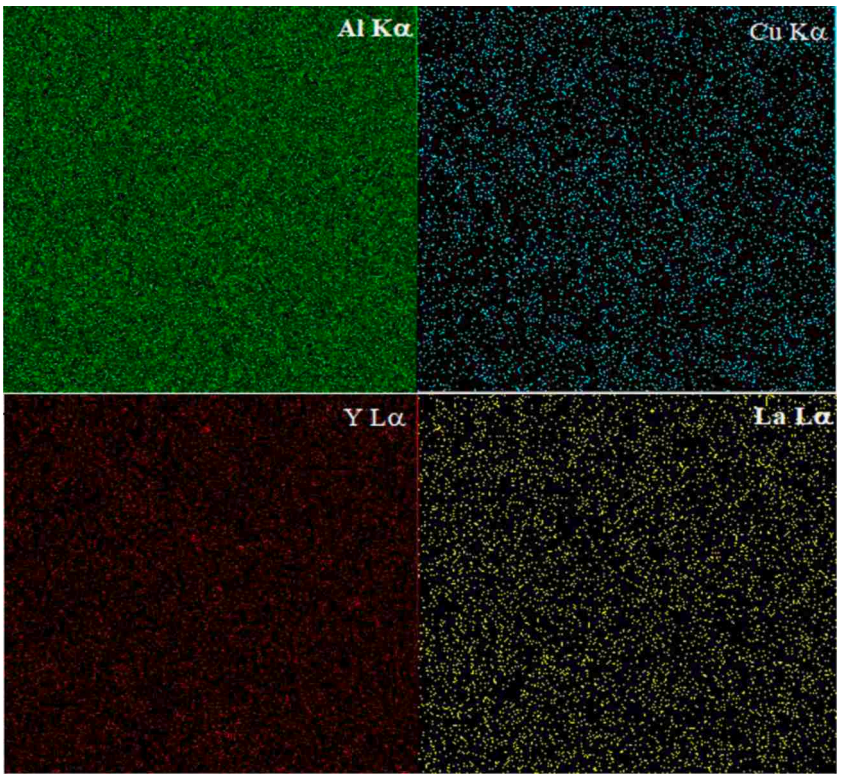

Fig. 6. X-ray mapping images of the bulk $Al_{86}Cu_6Y_6La_2$ alloy.

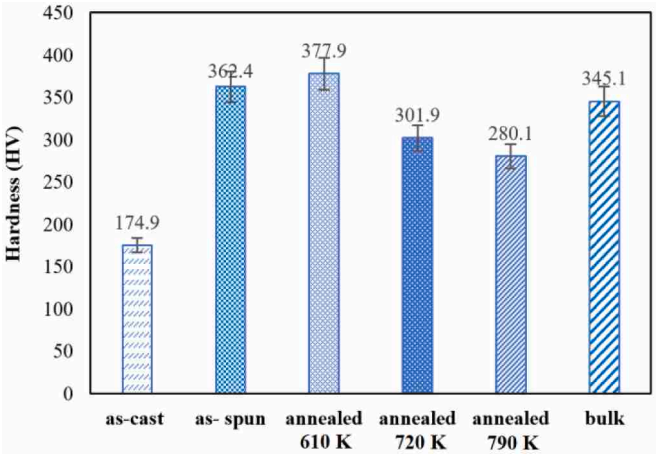

Fig. 7. Vickers hardness (HV) of the $Al_{86}Cu_6Y_6La_2$ alloy at different conditions (as- cast, as- spun, annealed and hot pressed).

$$\ln\left(\frac{\beta}{T_p^2}\right) = \left(-\frac{E_a}{RT_p}\right) + C(\text{Kissinger}) \quad (1)$$

$$\ln\beta = \frac{-1.0516E_a}{RT_p} + C(\text{Ozawa}) \quad (2)$$

$$\ln\left(\frac{\beta}{T_p - T_0}\right) = \left(-\frac{E_a}{RT_p}\right) + C(\text{Augis and Bennett}) \quad (3)$$

$$\ln(\beta) = \left(-\frac{E_a}{RT_p}\right) + C(\text{Moynihan}) \quad (4)$$

In the formulas, β is the heating rate, T_p is the peak temperature, E_a is the apparent activation energy,T_0 is the initial temperature of DSC analysis and C is a constant.

Figs. 9a-d show the Kissinger, Ozawa, Aguis & Bennet and Moynihan graphs for the primary, secondary and third crystallization of the $Al_{86}Cu_6Y_6La_2$ amorphous alloy, respectively. The activation energies E_a can be obtained from the straight-line slope achieved at three various heating rates (10, 15 and 20 K.min^{-1}) which are represented in Table 3. The results show that E_a for the primary, secondary and tertiary crystallization are in the range of about 254- 267 KJ.mol^{-1}, 198–203 KJ.mol^{-1} and 181- 186 KJ.mol^{-1}, respectively indicating that the reaction order is nearly to unity.

The crystallization process of the amorphous materials can describe by the Johnson Mehl Avrami (JMA) principle which has been extended to express the kinetics of crystallization in non-isothermal conditions [39–40]:

$$\ln\left[-\ln(1-X)\right] = -n\ln\beta + \ln K(T) \quad (5)$$

X is the volume fraction of the crystallized phase, t is the annealing time, β is the heating rate, n is the Avrami exponent and K is an Arrhenius reaction rate, which can be obtained from:

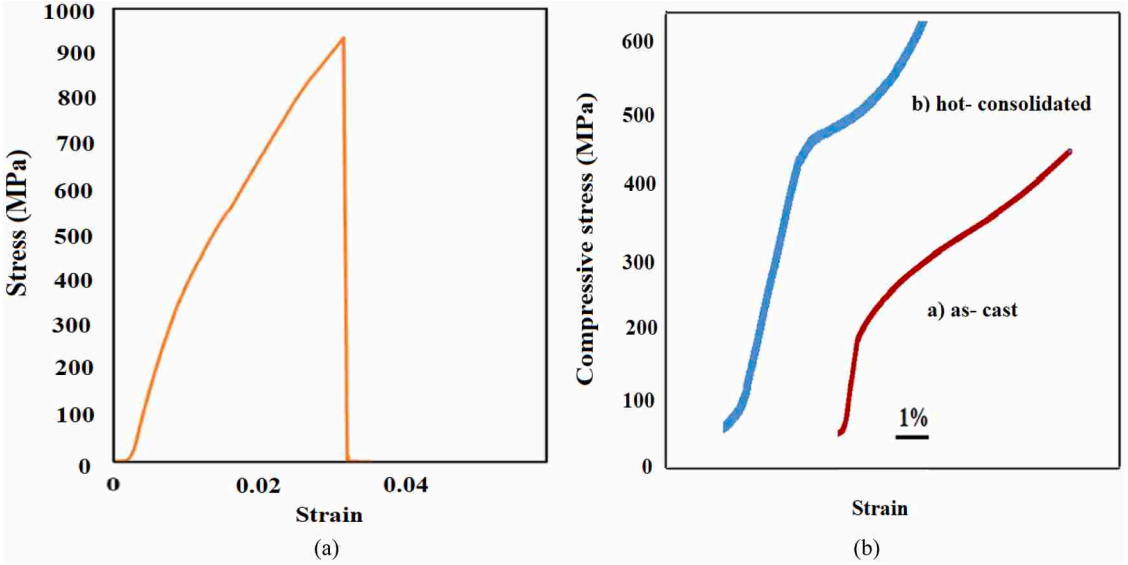

Fig. 8. (a) Tensile stress – strain curve for RS ribbons (room temperature) and (b) stress –strain curve for compression test of the consolidated bulk sample.

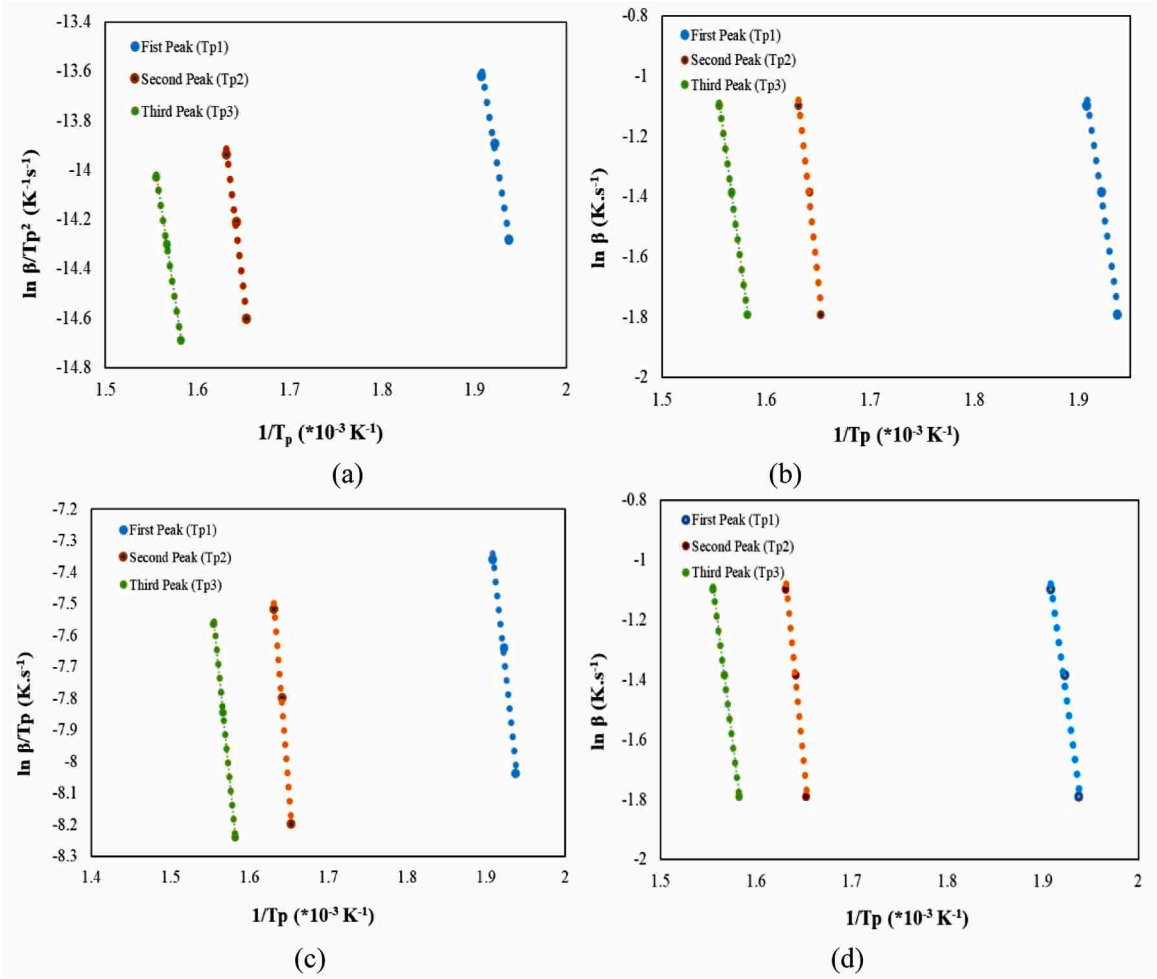

Fig. 9. (a) Kissinger, (b) Ozawa, (c) Augis & Bennett and (d) Moynihan methods for the first, second and third crystallization stages of the $Al_{86}Cu_6Y_6La_2$ metallic glass.

Table 3
Activation energies of each crystallization reaction are calculated by different methods for $Al_{86}Cu_6Y_6La_2$ alloy.

	Activation energies (KJ.mol^{-1})			
	Kissinger	Ozawa	Aguis & Bennett	Moynihan
First peak	257±107,078	254±12	262±13	267 ± 11
Second peak	202±8	203±9	198±6	203±9
Third peak	186±4	185±5	181±8	185±6

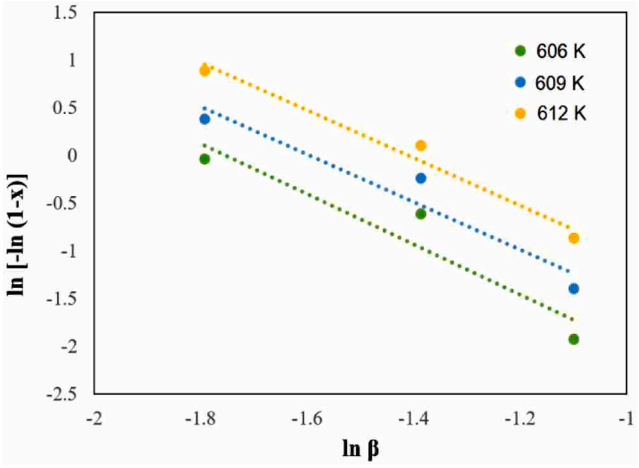

Fig. 10. Avrami plots of the $Al_{86}Cu_6Y_6La_2$ alloy for primary crystallization at various temperatures.

Table 4
Avrami index values for the primary crystallization reaction of the $Al_{86}Cu_6Y_6La_2$ alloy.

	Temperature (K)			Average
	606	609	612	
Avrami index	2.7	2.5	2.5	2.6 ± 0.1

$$K(T) = A \exp\left(\frac{-E_a}{RT}\right) \quad (6)$$

In this equation; A, Ea, T and R, are the frequency factor, the appearance activation energy for crystallization, temperature, and the gas constant, respectively. The slope of the straight lines in Figs. 9 yields Avrami exponent n which are shown in Fig. 10 and also Table 4. Temperatures between 606 K and 612 K (corresponding to the first DSC peak) yields n ranging from 2.49 to 2.63. According to the average Avrami exponent (n ~ 2.6), it can be found that the growth process of the primary crystallization of the $Al_{86}Cu_6Y_6La_2$ amorphous alloy is controlled by a 3D diffusion process and nucleation rates is reducing one. Although the nucleation process conducts the formation of a primary nano-sized phase, the growth process determines the size and morphology of the precipitated phases. Large RE (Y and La) atoms with small diffusivity for solute atoms suppresses the growth process and the movement of atoms decreases even more as the results of impingement. Therefore, it is preferred to precipitate single fcc-Al in the glassy matrix during the first reaction.

The volume fraction of the crystallization α, can be calculated from the fractional area of the DSC exothermic peak: [41–42]:

$$\alpha = \frac{\int_{T0}^{T}(dH/dT)\,dT}{\int_{T0}^{T_\infty}(dH/dT)dT} \quad (7)$$

Where; T_0, T_∞ and dH/dT are the initial temperatures, temperature at the end of each reaction peak and heat capacity of the alloy at constant pressure, respectively. The volume fraction (α) of the primary crystallized phase of the DSC curve at various heating rates are shown at Fig. 11 (a). All curves show a conventional sigmoid order and the crystallization occurs with a smaller rate at low annealing temperature. These sigmoidal *S* type curves confirm that the nucleation and growth process conducts the crystallization of the studied amorphous alloy, which usually consists of three steps [43]: Initially, the crystallization of the alloy is dominated by formation of the nuclei at low volume fractions; therefore, there is a low rate of crystallization process. Then, increasing the volume fraction of the crystallized phase decreases the free energy because of the crystals formation, and interface energy (crystals and matrix) enhances the rate of the crystallization process. Finally, the interface energy reduces which leads to decrease the rate of the crystallization.

To every crystallization peak (peak 1, and peak 2) at varied heating rates (10, 15, and 20 Kmin^{-1}), Fig. 7 depicts the change of the crystallized volume fraction a with temperature. With the increasing

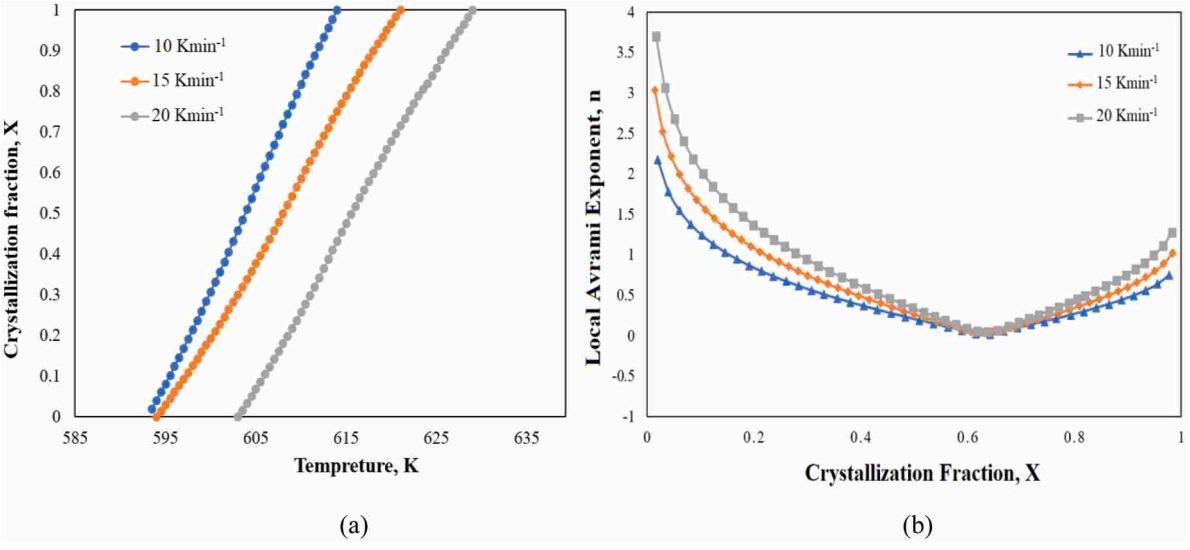

Fig. 11. (a) Crystalized fraction (X) - T for the primary crystallization and (b) local Avrami exponent curves at different heating rates (10, 15 and 20 Kmin^{-1}).

temperature, the crystalline volume fraction clearly shows a quasi "S" shape curve. In most cases, the crystallization of a "S" form may be broken down into three steps: For starters, the crystallization procedure of the alloy is mostly regulated by nucleation for low crystallized volume fractions, and the crystallization procedure of the alloy is mainly controlled by nucleation for high crystallized volume fractions.

The local Avrami exponent is depicted in Fig. 11. for the $Al_{86}Cu_6Y_6La_2$ alloy at various heating rates. When crystallization first begins, the local Avrami exponent is usually quite large. It begins to fall at the beginning of the crystallization process, then stabilizes before the intermediate stage ($0.3<X<0.8$) rising sharply at the end. There was a discrepancy between the Avrami exponent's initial and final values during crystallization. The Avrami exponents rise abnormally at high crystalline volume percentages due to inhomogeneous nuclei in amorphous ribbons and inhomogeneous nucleation in the crystallization procedure. When the crystallization process is in its middle stage, the local Avrami exponent appears to be stable, which explains why the nuclei develop to a noticeable size.

4.2. Microstructures of as- cast, as-spun and P/M materials

The microstructure of the as-cast, as-spun, annealed and consolidated samples can be shown in Figs. 4 and 5. Although, the microstructure of the as-cast $Al_{86}Cu_6Y_6La_2$ sample consists of the coarse eutectic phase, blocky regions of α-Al primary phase and some rod-shaped dark regions (intermetallic phases) rich in Cu and RE (Y, La) were the dominant feature in ingot specimens (Fig. 4a), the structure of the specimen produced by melt spinning indicates fine microstructure (Fig. 5). There is not any crystalline phase in the matrix indicating the fully amorphous structure. This can also be approved with the XRD patterns (Fig. 1b). Rapid solidification results in enhanced solid solubility of alloying elements, considerable increase in chemical homogeneity and formation of metallic glasses. In addition, more constituents in an alloy system decreases the tendency of an ordered structure formation due to the complexity of the crystals. Fine nano-sized homogeneously distributed α-Al crystalline phases, which have an equiaxial shape, can be observed in an amorphous matrix during primary crystallization of the alloy after heating the flakes continuously into about the end point of the first DSC peak. Growth rate at the fronts of the crystal growth can be inhibited by large RE (Y, La) atoms, which have slow diffusing nature. Therefore, heating at this temperature results in the nanocrystalline/amorphous composite material formation. Moreover, the GFA of Al–TM–RE alloys, is influenced by the strong reactivity between Al and TM atoms as the key mechanism controlling parameter. RE atoms (Y, La) with the randomly distributed order can stabilize the Al-Cu clusters [44].

Fig. 4d shows the optical micrograph of the bulk samples hot consolidated at the condition of $T = 723$ K, $P = 700$ MPa which leads to full densified $Al_{86}Cu_6Y_6La_2$ compact samples. FE-SEM image (Fig. 5e) of the bulk sample sintered at this condition shows bright agglomerates and black rod-like regions with nm- sized dimensions. X-ray mapping analysis of bulk sample (Fig. 6) suggests the black particles to be nano-sized Al grains with average size of 164 nm and bright particles which are rich in Cu, Co, Y and La and may corresponding to the intermetallic compounds like Al_3Y_5, Al_3Y, $AlCu_3$, Al_3Y_5 and AlCu observed by XRD (Fig. 3). Considering the width of the XRD peaks, it is suggested the dimensions of the phases formed are in the range of nano or ultra-fine.

4.3. Mechanical properties

The hardness results of the $Al_{86}Cu_6Y_6La_2$ alloy at as- cast, as- spun and after HP at $T = 723$ K and $P = 700$ MPa in Fig. 7 show the amorphous alloy indicates the hardness value (~ 362.4) more than two times that of conventional cast one (~174.9 HV). The extended solubility of elements in the matrix as the results of rapid solidification process, which leads to formation of metallic glasses, can contribute to enhanced microhardness of the rapidly solidified ribbons. The hardness changes largely after heat treatment of the amorphous $Al_{86}Cu_6Y_6La_2$ ribbons related to the different crystallization products. The fcc-Al nanocrystals formation during isochronal annealing at 610 K effects significantly on the enhancement of the hardness (~377.9 Hv). In the other words, the amorphous ribbons after heat treatment at about end temperature of the first reaction peak, shows a gradual increase in the microhardness, attributed to the crystallization onset: [amorphous]→ [amorphous+ α-Al]. The residual amorphous matrix is enriched in solute content which is an important factor in the hardening during annealing [39,40]. In addition, nano-sized α-Al nanocrystals distributed evenly in the amorphous matrix enhance the hardness by precipitation hardening during the primary reaction. Also, the hardness of the $Al_{86}Cu_6Y_6La_2$ amorphous alloy after the second DSC reaction decreases (~301.9). Formation of some weak intermetallic compounds and Al particles growth during the heat- treatment may lead to decrease of hardness. Complete crystallization of the amorphous matrix may also contribute to decrease the hardness after the third crystallization stage. Moreover, the bulk consolidated sample synthesized at 723 K and $P = 700$ MPa shows the hardness of about 345.1 HV which is more than two times that of conventional cast ones. Rapid solidification process and then formation of nano-size precipitates results in ultra-fine microstructure in the final bulk sample. The ultra-fine microstructure produced by melt spinning and hot consolidation can have a significant effect on the mechanical properties. The completely bulk sample produced by consolidation cannot be achieved without full devitrification resulting in enhanced mechanical properties. The mechanical properties of materials are influenced by hardness, strength and plastic strain. The tensile and compression tests were performed on the amorphous $Al_{86}Cu_6Y_6La_2$ RS ribbons and hot consolidated samples, respectively (Fig. 8). During the tensile test, the ribbons show YS of 680±21 and UTS of 910 ± 18 MPa and small specific plastic strain. This high strength level is due to its non-crystalline structure with no type of any defects (such as dislocations) which limit the strength of crystalline alloys.

Compression deformation of the bulk sample consolidated at pressing conditions of $T = 723$ K and $P = 700$ MPa, results in the yield strength of 460 ± 10 MPa, and a plastic strain of about 4 pct. Whereas, the as- cast sample indicates a yield strength of 184 ± 10 MPa and about 10 pct plastic strain. Structural refinement due to RS and ultra-fine intermetallic phases which are distributed uniformly together with nanocrystalline Al particles lead to such high strength enhancement. Crystallization entirely and formation of a network of fcc-Al interconnected partially or fully lead to increase the strength and hardness. However, the plastic deformation decreases. Therefore, high strength Al-based materials can be obtained through the consolidation of the amorphous alloys. Based on the microstructure and techniques of consolidation, it is possible to control the mechanical properties of the bulk materials.

4. Conclusion

1 The $Al_{86}Cu_6Y_6La_2$ alloy at as-spun condition has a fully amorphous structure. Annealing of the as-spun ribbons at different temperatures (610, 720 and 790 K) corresponding to each DSC stage shows different crystallization products. The first crystallization reaction corresponds to α-Al nanoparticles formation; whereas, the matrix is decomposed into different intermetallic compounds (Al_3Y, $AlCu_3$, AlCu and Al_3Y_5) after complete crystallization.

2 According to the DSC analysis, the onset crystallization temperatures and ΔT_X of $Al_{86}Cu_6Y_6La_2$ amorphous ribbons for different heating rates, are in the range of 596- 765 K and 24–25 K respectively, which shows high thermal stability and GFA of the produced amorphous alloy.

3 The activation energies E_a estimated from Kissinger, Ozawa, Aguis & Bennet and Moynihan methods for the primary, secondary and tertiary crystallization of the $Al_{86}Cu_6Y_6La_2$ amorphous alloy, are in the

range of about 254- 267 KJ.mol^{-1}, 198–203 KJ.mol^{-1} and 181- 186 KJ.mol^{-1}, respectively indicating the high thermal stability of the alloy. Moreover, the average Avrami exponent (n ~ 2.6) indicates that the growth of the amorphous alloy during primary crystallization is controlled by a three-dimensional process.

4 The $Al_{86}Cu_6Y_6La_2$ alloy at as- spun condition indicates the hardness value (~ 362.4) more than two times that of conventional cast one (~174.9 HV) due to extended solid solubility of the elements. The hardness reaches to ~377.9 Hv after the primary crystallization of fcc-Al nanocrystals at 610 K due to the precipitation hardening. However, after the second DSC peak, the hardness decreases (~301.9) as the result of some weak intermetallic compound formation, Al particles growth and complete devitrification of the amorphous matrix.

5 HP consolidated sample synthesized at 723 K and $P = 700$ MPa shows the hardness of about 345.1 HV which is more than two times that of conventional cast ones. The bulk sample indicates compression strength of 460 ± 10 MPa, and a plastic strain of about 4 pct. The ultra-fine microstructure induced by the rapid solidification process and hot consolidation has a significant effect on the mechanical properties.

CRediT authorship contribution statement

M. Dadashi: Formal analysis, Investigation, Validation. **M. Salehi:** Supervision, Conceptualization, Methodology, Formal analysis, Validation, Writing – original draft, Writing – review & editing. **S.G. Shabestari:** Conceptualization, Methodology, Writing – review & editing.

Declaration of Competing Interest

The authors declare that they have no known competing financial interests or personal relationships that could have appeared to influence the work reported in this paper.

This research did not receive any specific grant from funding agencies in the public, commercial, or not-for-profit sectors.

Data availability

Data will be made available on request.

References

[1] K.B. Surreddi, S. Scudino, M. Sakaliyska, K.G. Prashanth, D.J. Sordelet, J. Eckert, Crystallization behavior and consolidation of gas-atomized $Al_{84}Gd_6Ni_7Co_3$ glassy powder, J. Alloys Compd. 491 (2010) 137–142, https://doi.org/10.1016/j.jallcom.2009.10.178.

[2] A. Sahu, R.S. Maurya, T. Laha, Non-isothermal crystallization behavior of $Al_{86}Ni_8Y_6$ and $Al_{86}Ni_6Y_{4.5}Co_2La_{1.5}$ melt-spun ribbons, milled ribbon particles and bulk samples consolidated by spark plasma sintering, Thermochim. Acta. 684 (2020), 178486, https://doi.org/10.1016/j.tca.2019.178486.

[3] M. Salehi, S.G. Shabestari, S.M.A. Boutorabi, Nanostructure evolution and mechanical properties of rapidly solidified Al–Ni–RE (Y, Ce) alloys, Mater. Sci. Eng. A. 586 (2013) 407–412, https://doi.org/10.1016/j.msea.2013.08.040.

[4] M. Salehi, S.G. Shabestari, S.M.A. Boutorabi, Nanostructure and mechanical properties of bulk Al86Ni6Y6Ce2 alloy produced by hot consolidation of amorphous melt-spun flakes, Metall. Mater. Trans. 45 (2014) 6344–6351, https://doi.org/10.1007/s11661-014-2542-4.

[5] Y. Wang, Y. Liu, Y. Li, B. An, G. Cao, S. Jin, Y. Sun, W. Wang, Crystallization of Al-based amorphous alloys in good conductivity solution, J Mater Sci Technol 30 (2014) 1262–1270, https://doi.org/10.1016/j.jmst.2014.10.003.

[6] Y. Shen, J.H. Perepezko, Al-based amorphous alloys: glass-forming ability, crystallization behavior and effects of minor alloying additions, J. Alloys Compd. 707 (2017) 3–11, https://doi.org/10.1016/j.jallcom.2016.11.079.

[7] S.H. Wang, X.F. Bian, Effect of Si and Co on the crystallization of Al–Ni–RE amorphous alloys, J. Alloys Compd. 453 (2008) 127–130, https://doi.org/10.1016/j.jallcom.2006.11.056.

[8] J.I. Hyun, C.I. Kim, S.W. Nam, W.T. Kim, D.H. Kim, Nanoscale phase separation and microstructure evolution during crystallization in Al-Si-Ni amorphous alloy, Mater. Des. 192 (2020), 108719, https://doi.org/10.1016/j.matdes.2020.108719.

[9] D.H. Kim, W.T. Kim, D.H. Kim, Formation and crystallization of Al–Ni–Ti amorphous alloys, Mater. Sci. Eng. A 385 (2004) 44–53, https://doi.org/10.1016/j.msea.2004.04.016.

[10] F.G. Cuevas, S. Lozano-Perez, R.M. Aranda, E.S. Caballero, Crystallization of amorphous Al-Sm-Ni-(Cu) alloys, Intermetallics 112 (2019), 106537, https://doi.org/10.1016/j.intermet.2019.106537.

[11] E.R. Wang, X.D. Hui, S.S. Wang, Y.F. Zhao, G.L. Chen, Microstructure and mechanical properties of Al–Si–Ni–Ce alloys prepared by gas-atomization spark plasma sintering and hot-extrusion, Mater. Sci. Eng. A 528 (2011) 5764–5771, https://doi.org/10.1016/j.msea.2011.03.102.

[12] G.Q. Xie, D.V. Louzguine-Luzgin, A. Inoue, Formation and properties of two-phase bulk metallic glasses by spark plasma sintering, J. Alloys. Compd. 509 (2011) S214–SS18, https://doi.org/10.1016/j.jallcom.2010.10.007.

[13] H.S. Kim, S.I. Hong, A model of the ductile–brittle transition of partially crystallized amorphous Al–Ni–Y alloys, Acta Mater 47 (1999) 2059–2066, https://doi.org/10.1016/S1359-6454(99)00088-9.

[14] M. Kubota, P. Cizek, W.M. Rainforth, Properties of mechanically milled and spark plasma sintered Al–15 at.% MgB2 composite materials, Compos Sci Technol 68 (2008) 888–895, https://doi.org/10.1016/j.compscitech.2007.08.010.

[15] C.C. Koch, Nanostructured Materials Processing, Properties and Applications, 2nd ed., William Andrew publishing, Norwich, NY, 2007.

[16] Z.H. Huang, J.F. Li, Q.L. Rao, Y.H. Zhou, Effects of La content on the glass transition and crystallization process of Al–Ni–La amorphous alloys, Intermetallics 15 (2007) 1139–1146, https://doi.org/10.1016/j.intermet.2007.02.001.

[17] S.J. Hong, P.J. Warren, B.S. Chuna, Nanocrystallization behaviour of Al–Y–Ni with Cu additions, Mater. Sci. Eng. A 304–306 (2001) 362–366, https://doi.org/10.1016/S0921-5093(00)01480-5.

[18] P. Yu, K.B. Kim, J. Das, F. Baier, W. Xu, J. Eckert, Fabrication and mechanical properties of Ni–Nb metallic glass particle-reinforced Al-based metal matrix composite, Scr. Mater. 54 (2006) 1445–1450, https://doi.org/10.1016/j.scriptamat.2006.01.001.

[19] S. Scudino, K.B. Surreddi, S. Sager, M. Sakaliyska, J.S. Kim, W. Löser, J. Eckert, Production and mechanical properties of metallic glass-reinforced Al-based metal matrix composites, J. Mater. Sci. 43 (2008) 4518–4526, https://doi.org/10.1007/s10853-008-2647-5.

[20] K.G. Prashanth, S. Scudino, B.S. Murty, J. Eckert, Crystallization kinetics and consolidation of mechanically alloyed Al70Y16Ni10Co4 glassy powders, J. Alloys Compd. 477 (2009) 171–177, https://doi.org/10.1016/j.jallcom.2008.10.055.

[21] W.J. Botta, C. Triveno Rios, R.D. Sa Lisboa, A.R. de Andrade, M.F. de Oliveira, C. Bolfarini, C.S. Kiminami, Crystallization behaviors of Al-based metallic glasses: compositional and topological aspects, J. Alloys Compd. 483 (2009) 89–93, https://doi.org/10.1016/j.jallcom.2008.08.122.

[22] M. Wollgarten, K.L. Sahoo, J. Haug, J. Banh, Influence of La on the crystallization behavior of amorphous $Al_{94-x}Ni_6La_x$(x=4–7) alloys, Mater. Sci. Eng. A. 449–451 (2007) 1049–1051, https://doi.org/10.1016/j.msea.2006.02.351.

[23] Z.C. Zhong, X.Y. Jiang, A.L. Gree, Nanocrystallization in Al-based amorphous alloys, Philos. Mag. B. 76 (1997) 505–510, https://doi.org/10.1080/01418639708241116.

[24] M. Salehi, S.G. Shabestari, S.M.A. Boutorabi, Nano-crystal development and thermal stability of amorphous Al–Ni–Y–Ce alloy, J. Non-Cryst. Solids 375 (2013) 7–12, https://doi.org/10.1016/j.jnoncrysol.2013.04.059.

[25] M.A. Munoz-Morris, S. Surinach, L.K. Varga, M.D. Baro, D.G. Morris, The influence of composition and low temperature annealing on hardness and ductility of rapidly solidified Al–Ni–Ce alloys, Scr. Mater. 47 (2002) 31–37, https://doi.org/10.1016/S1359-6462(02)00093-3.

[26] A.P. Kumar, V.M.S Muthaiah, S. Mula, Effect of Nb, Y and Zr on thermal stability of nanocrystalline Al-4.5wt.% Cu alloy prepared by mechanical alloying, J. Alloys Compd. 722 (2017) 617–627, https://doi.org/10.1016/j.jallcom.2017.06.089.

[27] M.G. Khomutov, S.M. Amer, R. Yu. Barkov, M.V. Glavatskikh, A. Yu. Churyumov, A.V. Pozdniakov, Hot Deformation Behavior of Novel Al-Cu-Y(Er)-Mg-Mn-Zr Alloys, Metals (Basel) 11 (2021) 1521, https://doi.org/10.3390/met11101521.

[28] Y. He, G.M. Dougherty, G.J. Shiflet, S.J. Poon, Unique metallic glass formability and ultra-high tensile strength in Al-Ni-Fe-Gd alloys, Acta Mater 41 (1993) 337–343, https://doi.org/10.1016/0956-7151(93)90064-Y.

[29] M.G. Khomutov, S.M. Amer, R.Y. Barkov, M.V. Glavatskikh, A.Y. Churyumov, A. V. Pozdniakov, Hot deformation behavior of novel Al-Cu-Y(Er)-Mg-Mn-Zr alloys, Metals 11 (2021) 1521, https://doi.org/10.3390/met11101521.

[30] C.T. Rios, S. Surinach, M.D. Baro, C. Bolfarini, W.J. Botta, C.S. Kiminami, Glass forming ability of the Al–Ce–Ni system, J. Non-Cryst. Solids 354 (2008) 4874–4877, https://doi.org/10.1016/j.jnoncrysol.2008.04.035.

[31] A. Inoue, Stabilization of metallic supercooled liquid and bulk amorphous alloys, Acta mater 48 (2000) 279–306, https://doi.org/10.1016/S1359-6454(99)00300-6.

[32] P.J. Squire, I.T.H. Chang, Development of rapidly solidified Al–Y–Ni-based alloys, Mater. Sci. Eng. A 449–451 (2007) 1009–1012, https://doi.org/10.1016/j.msea.2006.02.274.

[33] Z. Huang, J. Li, Q. Rao, Y. Zhou, Dependences of the crystallization behavior of Al–Ni–La amorphous alloys on La and Ni contents, J. Non-Cryst. Solids 354 (2008) 1671–1677, https://doi.org/10.1016/j.jnoncrysol.2007.10.017.

[34] M. Salehi, S.G. Shabestari, Nanostructure evolution, thermal stability an d hardness of amorphous Al-Cu-Y (Co, La) (at.%) alloys, J. Non-Cryst. Solids 589 (2022), 121663, https://doi.org/10.1016/j.jnoncrysol.2022.121663.

[35] H.E. Kissinger, Variation of peak temperature with heating rate in differential thermal analysis, J. Res. Natl. Bur. Stand. 57 (1956) 2712, https://doi.org/10.6028/jres.057.026.

[36] H.E. Kissinger, Reaction kinetics in differential thermal analysis, Anal. Chem. 29 (1957) 1702–1706, https://doi.org/10.1021/ac60131a045.
[37] M. Fatmi, B. Ghebouli, M.A. Ghebouli, T. Chihi, M.A. Hafiz, The kinetics of precipitation in Al-2.4 wt% Cu alloy by Kissinger, Ozawa, Bosswel and Matusita methods, Phys. B 406 (2011) 2277–2280, https://doi.org/10.1016/j.physb.2011.03.053.
[38] J. Augis, J. Bennett, Calculation of the Avrami parameters for heterogeneous solid state reactions using a modification of the Kissinger method, J. Therm. Anal. Calorim. 13 (1978) 283–292, https://doi.org/10.1007/BF01912301.
[39] D.W. Henderson, Thermal analysis of non-isothermal crystallization kinetics in glass forming liquids, J. Non-Cryst. Solids. 30 (1979) 301–315, https://doi.org/10.1016/0022-3093(79)90169-8.
[40] D.W. Henderson, Experimental analysis of non-isothermal transformations involving nucleation and growth, J. Therm. Anal. Calorim. 15 (1979) 325–331, https://doi.org/10.1007/BF01903656.
[41] T. Paul, A. Loganathan, A. Agarwal, S.P. Harimkar, Kinetics of isochronal crystallization in a Fe-based amorphous alloy, J. Alloys. Compd. 753 (2018) 679–687, https://doi.org/10.1016/j.jallcom.2018.04.133.
[42] X.F. Lu, J.N. Hay, Isothermal crystallization kinetics and melting behavior of poly (ethylene terephthalate), Polymer 42 (2001) 9423–9431, https://doi.org/10.1016/S0032-3861(01)00502-X.
[43] Q. Dong, P. Song, J. Tan, X.M. Qin, C.J. Li, P. Gao, Z.X. Feng, M. Calin, J. Eckert, Non-isothermal crystallization kinetics of a Fe-Cr-Mo-B-C amorphous powder, J. Alloys. Compd. 823 (2020), 153783, https://doi.org/10.1016/j.jallcom.2020.153783.
[44] K. Song, X. Bian, X. Lv, J. GuO, G. Li, M. Xie, Compositional dependence of glass-forming ability, medium-range order, thermal stability and liquid fragility of Al–Ni–Ce-based amorphous alloys, Mater. Sci. Eng. A 506 (2009) 87–93, https://doi.org/10.1016/j.msea.2008.11.043.